Research Article

Cobalt single atom site catalysts with ultrahigh metal loading for enhanced aerobic oxidation of ethylbenzene

Yu Xiong[1,2,§], Wenming Sun[3,§], Yunhu Han[4,§], Pingyu Xin[2], Xusheng Zheng[5], Wensheng Yan[5], Juncai Dong[6], Jian Zhang[2], Dingsheng Wang[2] (✉), and Yadong Li[2]

[1] Department of Chemistry and Chemical Engineering, Central South University, Changsha 410083, China
[2] Department of Chemistry, Tsinghua University, Beijing 100084, China
[3] China College of Science, China Agricultural University, Beijing 100193, China
[4] Institute of Flexible Electronics, Northwestern Polytechnical University, Xi'an 710072, China
[5] National Synchrotron Radiation Laboratory, University of Science and Technology of China, Hefei 230029, China
[6] Beijing Synchrotron Radiation Facility, Institute of High Energy Physics, Chinese Academy of Sciences, Beijing 100084, China
[§] Yu Xiong, Wenming Sun, and Yunhu Han contributed equally to this work.

ABSTRACT

The oxidation of hydrocarbons to produce high value-added compounds (ketones or alcohols) using oxygen in air as the only oxidant is an efficient synthetic strategy from both environmental and economic views. Herein, we successfully synthesized cobalt single atom site catalysts (Co SACs) with high metal loading of 23.58 wt.% supported on carbon nitride (CN), which showed excellent catalytic properties for oxidation of ethylbenzene in air. Moreover, Co SACs show a much higher turn-over frequency (19.6 h^{-1}) than other reported non-noble catalysts under the same condition. Comparatively, the as-obtained nanosized or homogenous Co catalysts are inert to this reaction. Co SACs also exhibit high selectivity (97%) and stability (unchanged after five runs) in this reaction. DFT calculations reveal that Co SACs show a low energy barrier in the first elementary step and a high resistance to water, which result in the robust catalytic performance for this reaction.

KEYWORDS

single atom site, high-loading catalysts, heterogeneous catalysts, ethylbenzene oxidation

1 Introduction

Acetophenone and its derivatives are vital chemical intermediates in the synthesis of various pharmaceuticals, agrochemicals, perfumes, etc [1–3]. Traditional synthetic processes of acetophenone, using Friedel–Crafts acylation or oxidizing styrene by KMnO$_4$, lead to the production of a large amount of corrosive and toxic wastes [4]. Currently, selective oxidation especially aerobic oxidation of ethylbenzene to obtain acetophenone has attracted much more interests from researchers. Air is the most convenient, cheap, moderate and environmentally benign oxidant in this process, while air is also unreactive and hard to activate, especially to the strong C–H bond of alkylaromatics. Nowadays, several efforts have been employed to optimize the catalytic system in the oxidation of ethylbenzene with oxygen especially the oxygen in air [5–10]. Whereas, some important subjects are still unsettled, such as: (a) the use of environmental-unfriendly inhibitors (peroxides, N-hydroxyphthalimide, etc.) or corrosive solvent (acetic acid), (b) the oxygen in air can hardly be activated, (c) dependence of noble metals. Therefore, catalytic oxidation of ethylbenzene with air as the only oxidant is still a challenge and the exploration of novel catalysts to improve the catalytic performance is essential.

Recently, metal single atom sites embedded on CN supports (M SACs /CN) have drawn a lot of attentions from researchers,

because the highly active M-N$_x$ (M = Fe, Co, Ni, Pt, Ir, Er, etc.; X = 2–6) moieties always show excellent performances in photo-catalysis, eletrocatalysis, and organocatalysis etc. [11–30]. Among those M SACs/CN, Co SACs/CN show exceptional catalytic properties [31–39]. For example, Zhao and his co-workers synthesized Co-SA/AC@N-CNTs with CoN$_x$ moiety as active sites and obtained excellent catalytic properties towards selective hydrogenation of quinolines [33]. Fei et al. prepared single atomic Co on nitrogen-doped graphene, which showed robust activity in hydrogen evaluation reaction (HER) [39]. However, the potential catalytic properties and the further practical applications of Co SACs/CN are far from fully explored, because their relatively low metal loading brings about series of puzzles. On one hand, low metal loading in SACs causes low volumetric activity, which will enlarge the dosage of total catalysts and increase the volume of the reaction container in practical applications and thus results in high cost [40–42]. On the other hand, the high metal loading in catalysts increases the density of the active sites and accelerates the mass transfer in the reaction, which can enhance the reactivity of catalysts [43, 44].

Herein, we successfully synthesized Co SACs which possess a high metal loading of 23.58 wt.%. Moreover, Co SACs exhibit excellent catalytic performance towards oxidation of ethylbenzene in air. Specifically, Co SACs affords higher turnover-frequency (TOF; 19.6 h^{-1}), conversion (46%), selectivity (97%) and stability

(nearly unchanged after 5 cycles) than all of reported base metal catalysts under the same condition, while the as-obtained nanosized or homogeneous Co catalysts are inactive to this reaction.

2 Experimental details

2.1 Chemicals

$Co(NO_3)_2$ and dicyandiamide were purchased from Alfa Aesar Chemical Co. Ltd. (USA). Formaldehyde was purchased from Sinopharm Chemical Reagent Co. Ltd. (China). Ethylbenzene, n-dodecane and other organic compound were purchased from Acros organics (Belgium). The distilled water used in all experiments was obtained through ion-exchange and filtration. All of the chemicals used in this experiment were of analytical grade and used without further purification.

2.2 Synthesis of Co SACs

In a typical synthesis of Co SACs, dicyandiamide (59.47 mmol, 5 g), formaldehyde (59.47 mmol, 4.4 mL; 37 wt.% solution) and $Co(NO_3)_2·6H_2O$ (8.48 mmol; 2.47 g) were mixed in distilled water (ca. 25 mL). After vigorous stirring (5 min), the mixed solution was heated to about 100 °C and kept for more than 12 h to ensure the complete vaporization of the solvent. In the process, formaldehyde was polymerized with dicyandiamid and Co ions are coordinated with dicyandiamide-formaldehyde resin thoroughly. The purple solid was next heated in a tube furnace to 600 °C under Ar atmosphere for 120 min. Then the as-obtained dark brown solid cooled to room temperature and was heated to 400 °C under H_2/Ar (5%) atmosphere for 120 min. The as-obtained solid was denoted as Co SACs, which can be used directly without any post-treatment.

2.3 Synthesis of Co NPs/CN

Co NPs/CN was synthesized as previous reported [45]. In a typical procedure, $Co(NO_3)_2·6H_2O$ (0.546 g; 1.87 mmol) was dissolved in 15 mL methanol to form a clear solution, which was subsequently injected into 15 mL of methanol containing 2-methylimidazole (0.616 g; 7.5 mmol) under ultrasonic treatment for 10 min at room temperature. The mixed solution was then transferred into 50 mL Teflon-lined stainless-steel autoclaves and heated at 120 °C for 4 h. The as-obtained precipitates were centrifuged and washed with ethanol several times and dried in vacuum at 60 °C for overnight. The as-obtained purple powder was placed in a tube furnace and then heated to 800 °C for 3 h at the heating rate of 5 °C/min under flowing N_2 gas and then naturally cooled to room temperature to obtain the representative samples. The as-prepared products were directly used without any post-treatment.

2.4 Typical procedure of catalytic oxidation of alkylaromatics

In a typical oxidation, 1 mL alkylaromatics (calculated using a microliter syringe; 1,200 mg for fluorene) and 2 mg Co SACs (20 mg Co NPs/CN or Co-porphyrin) were added into a 10 mL Schelenk tube with a magnetic stirrer. The whole reaction system connected with air through a condenser. The reaction was performed at 120 °C for a desired time. After the completion of the reaction, internal standard (dodecane; 100 μL) was added to the liquid phase. The liquid mixture was collected by centrifugation and 10 mL ethyl acetate was added to the reaction system (dichloromethane was used for the oxidation of fluorene) for further GC-FID analysis.

2.5 Catalyst recycling test

The reaction mixture was centrifuged after the reaction finished and the liquid layer was then siphoned out by a microliter syringe. The residues were washed with 8 mL ethanol and ethyl acetate twice respectively. The as-obtained solid was centrifuged and dried in a vacuum for a whole night over 70 °C. Finally, the recovered Co SACs was used in the following reactions.

2.6 Characterizations

Powder X-ray diffraction patterns (XRD) were recorded with a Rigaku D/max 2500Pc X-ray powder diffractometer with monochromatized Cu Kα radiation (λ = 1.5406 Å). Transmission eletron microscopy (TEM) and scanning TEM (STEM) images were recorded by a Hitachi HT7700 working at 100 kV, and a FEI Tecnai G2 F20 S-Twin working at 200 kV, respectively. An ARM-200CF (JEOL, Tokyo, Japan) transmission electron microscope operated at 200 keV and equipped with double spherical aberration correctors (Cs) is used to take AC-HAADF-STEM images. The attainable resolution of the probe defined by the objective pre-field is 78 picometers. Inductively coupled plasma optical emission spectrometry (ICP-OES) was carried out on Thermo Fisher IRIS Intrepid Ⅱ. The element analysis test was performed on Eurovector EA3000. X-ray photoelectron spectroscopy (XPS) spectra were performed by a Thermo Fisher ESCALAB Scientific ESCALAB 250Xi XPS System. The N K-edge NEXAFS spectra were collected at BL12B station of National Synchrotron Radiation Laboratory (NRSL) in Hefei, China. The GC analysis was conducted on a Thermo Trace 1300 series GC with a FID detector using a capillary column (TR-5MS, from Thermo Scientific, length 30 m, i.d. 0.25 mm, film 0.25 μm).

3 Results and discussion

At first, Co SACs are fabricated via a facile strategy. Dicyandiamide was polymerized with formaldehyde to form dicyandiamide–formaldehyde resin and coordinated with Co precursors ($Co(NO_3)_2$) in one pot. The Co SACs are formed by pyrolyzing the Co-coordinated polymer in argon and H_2/Ar atmosphere respectively. From XRD pattern, we can see the only broad peak representing amorphous carbon nitride (CN) in Co SACs (Fig. S1 in the Electronic Supplementary Material (ESM)) [46]. The laminar structure of Co SACs can be observed in TEM (Fig. S2 in the ESM) and STEM (Fig. 1(a) and Fig. S3 in the ESM) images, from which no nanoparticles are detected. The thickness of Co SACs is about 3.6 nm, which is certified by atomic force microscope (AFM) measurement (Fig. S4 in the ESM). Energy-dispersive X-ray (EDX) elemental mapping analysis shows the homogeneous dispersion of C, N and Co in Co SACs (Fig. 1(b)). The aberration-corrected high-angle annular dark-field STEM (AC-HAADF-STEM) image is shown in Fig. 1(c). Since the clearly distinct Z-contrast between Co and C (N), the single atom Co sites can be identified by Z-contrast analysis (Fig. S5 in the ESM). The interatomic distance of adjacent Co sites is about 0.35–0.5 nm, further suggesting the ultra-high Co loading of Co SACs. More single atom Co sites in the enlarged AC-HAADF-STEM images are cycled to certify the non-existent of nanoparticles or clusters in Co SACs (Fig. 1(d) and Fig. S6 in the ESM). The Co loading in Co SACs is verified by ICP-OES, which reaches up to 23.58 wt.%. The element analysis test of Co SACs shows that the content of C, N, O and H is 26.4 wt.%, 39.1 wt.%, 1.7 wt.% and 9.9 wt.%, respectively. The high nitrogen content (the atomic ratio of C and N is about 1:1.27) is one of the reasons leading to the high density of cobalt atoms.
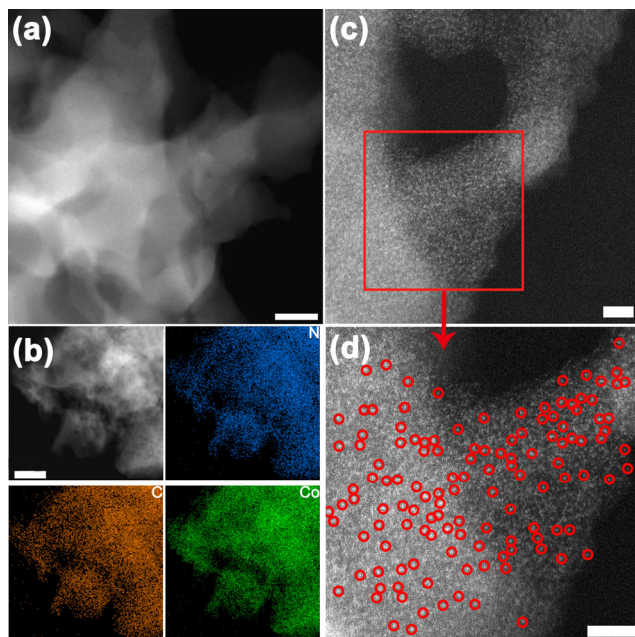
Figure 1 Characterizations of Co SACs. (a) STEM image of Co SACs; scale bar: 20 nm. (b) STEM images and corresponding EDX-mapping of Co SACs. ((c) and (d)) AC-HAADF-STEM and enlarged image of Co SACs; the single atom Co sites in (d) are highlighted by red circles; scale bars: 2 nm.

To confirm the local structure of Co sites in Co SACs, we performed extended X-ray absorption fine structure spectroscopy (EXAFS). From Co K-edge X-ray absorption near edge structure (XANES) spectra, we can see that the absorption edge of Co SACs is located near that of CoO, indicating the oxidation state of Co atoms in Co SACs is +2 (Fig. 2(a)). Co SACs display only one main peak at 1.50 Å in Fourier-transformed k^3-weithted EXAFS (FT-EXAFS) spectra, corresponding to the Co-N first coordination shell (Fig. 2(b)). Moreover, no visible Co–Co coordination peak is detected, which indicates no Co clusters or nanoparticles in Co SACs. Wavelet transform (WT) analysis was carried out to certify this result. We can see the intensity maximum at about 6.2 Å^{-1} that arises from Co–Co bond in Co foil, CoO and Co$_3$O$_4$ (Figs. 2(c), 2(e) and 2(f)), while only one intensity maximum at around 4.0 Å^{-1} is detected in Co SACs, which can be attributed to the first coordination shell of Co–N bond (Fig. 2(d)). The quantitative structural parameters of Co sites in Co SACs are obtained from EXAFS curve fitting (Figs. 2(g) and 2(h)). The corresponding EXAFS fitting parameters are shown in Table S1 in the ESM, from which we can see that the coordination number of center Co atoms is about 2.3 and the average bond length of Co SACs is 1.95 Å (Table S1 in the ESM). These results indicate that Co atoms are coordinated with two nitrogen atoms in Co SACs (the inset of Fig. 2(g) shows the corresponding model of atomic structure).

To illustrate the interaction between Co atoms and CN support, we measured XPS and near-edge X-ray absorption fine structure (NEXAFS) spectra of Co SACs. XPS survey spectrum shows that C, N, O and Co are the main components in Co SACs (Fig. S7 in the ESM). Co 2p XPS spectrum of Co SACs shows two main peaks at 796.0 and 780.6 eV with two satellite peaks at 785.4 and 802.1 eV, indicating the Co^{2+} species in Co SACs (Fig. 3(a)), which is consistent with results of XANES analysis. N 1s XPS spectrum of Co SACs (Fig. 3(b)) can be deconvoluted into two peaks with binding energies of 398.8 and 399.9 eV, which are attributed to pyridinic N and pyrrolic N [47]. C 1s XPS spectrum of Co SACs (Fig. 3(c))
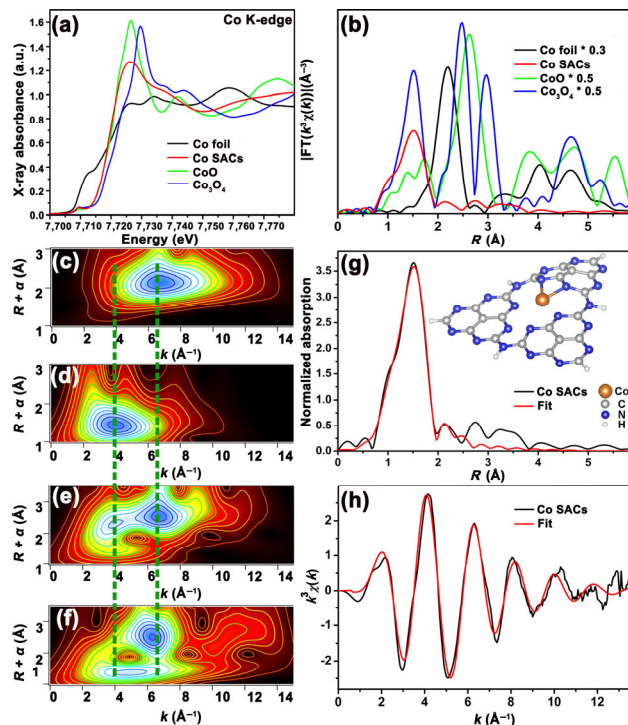

Figure 2 XAFS analysis of Co SACs. (a) XANES spectra and (b) FT-EXAFS at the Co K-edge of Co SACs, Co foil, CoO and Co$_3$O$_4$ respectively. (c)–(f) wavelet transform (WT) of Co foil (c), Co SACs (d), CoO (e) and Co$_3$O$_4$ (f) samples. EXAFS curve fitting of Co SACs at (g) R space and (h) k space. The inset of 2g is structure model of Co SACs.
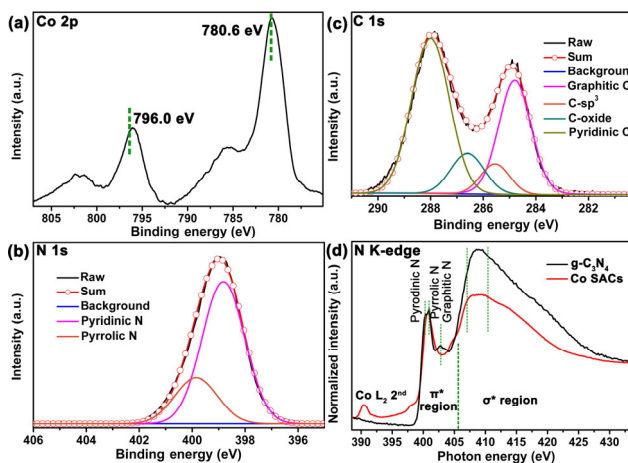

Figure 3 XPS and NEXAFS spectra. (a) Co 2p, (b) N 1s and (c) C 1s XPS spectra of Co SACs. (d) NEXAFS spectra of Co SACs and g-C$_3$N$_4$. The peak at 391 eV in (d) is related to the second-order photon excited Co L$_2$.

deconvolves into four peaks at 284.8, 285.5, 286.5 and 288.0 eV, which are appointed to the graphitic C (C–C), C-sp^3 (C–C$_3$ or C–N$_3$), C–oxide (C–O), and pyridinic C (C=N), respectively [48]. The only peak located at 531.4 eV can be detected in O 1s XPS spectrum of Co SACs, suggesting the form of O species in Co SACs is absorbed O$_2$ (Fig. S8 in the ESM) [49].

From N K-edge NEXAFS spectra of Co SACs and g-C$_3$N$_4$, we can see that g-C$_3$N$_4$ shows three main resonances in π* region (400.3 eV, pyridinic N; 401.0 eV, pyrrolic N and 402.8 eV, graphitic N). Resonance of graphitic N (402.8 eV) shows a huge decline for Co SACs (Fig. 3(d); other peaks are almost identical), indicating non-existence of graphitic N. In the σ* region of N K-edge NEXAFS spectra (~ 408 eV), Co SACs show a broader resonance than g-C$_3$N$_4$, which indicates the diversified length of C–N bonds [50, 51]. These results suggest the addition

of Co spices in CN support induces large number of defects. Defects, high nitrogen content combined with low coordination number of Co atoms endow Co SACs with ultra-high metal loading.

To explore the potential heterogeneous catalysts, we test the oxidation of ethylbenzene in air using Co SACs as catalysts. We surprisingly discovered that Co SACs showed extremely high catalytic performance (46% conversion and 97% selectivity) at 120 °C for 24 h (Table 1, Entry 1). The TOF value is as high as 19.6 h^{-1}, which is several times higher than other base metal catalysts ever known [4–6]. It should be highlighted that only a tiny amount of Co SACs (2 mg) is able to catalyze 1 mL ethylbenzene, which is attributed to the high loading of single atom sites. For comparison, Entry 2 and 3 in Table 1 show that Co nanoparticles/CN (Co NPs; TEM images and XRD pattern are shown in Figs. S9 and S10 in the ESM) and Co-porphyrin are inactive in this reaction. When the oxidation reaction is performed in nitrogen atmosphere, none detectable product is observed, which gives the evidence that air plays the key role in this reaction system (Table 1, Entry 4). When hydroquinone (a free radical scavenger) is added to the reaction, reaction is quenched, which indicates that the oxidation of ethylbenzene on Co SACs proceeds via a radical chain pathway (Table 1, Entry 5). The capability of recovering and reusing Co SACs shows that Co SACs is almost unchanged during five runs (Table 1, Entry 6). We collected the liquid phase of reaction mixture by centrifugation and analyzed the solution by ICP-OES. Only a slight amount of dissolved Co (Co: 6.45 ppm; 1.19% of the total cobalt in Co SACs) was detected. XRD patterns (Fig. S11 in the ESM) show no modification after catalytic test. TEM (Fig. S12 in the ESM), STEM (Fig. S13 in the ESM) images combined with EDS mapping (Fig. S14 in the ESM) further confirm that Co SACs is almost unchanged after catalytic reactions.

We further investigated the evolution of catalytic performance with reaction time over the oxidation of ethylbenzene in air to study the reaction kinetics. The plots in Fig. S15 in the ESM indicate the first-order kinetics of this reaction and the corresponding rate constant is shown in Fig. S16 in the ESM. The conversion reaches 62% and the selectivity is as high as 99% when we prolong the reaction time to 40 h. In most references, with the reaction time increases, the selectivity of acetophenone usually decreases and the yield of 1-phenylehanol increases [7, 52]. However, the yield of by-product (1-phenylethanol) decreases and the selectivity of acetophenone increases gradually with

the reaction time increase, which also indicates the high stability of Co SACs.

From Table S2 in the ESM, we can see the scope of substrates for oxidation of alkylaromatics using Co SACs catalyst under same condition. The oxidation of indan affords a conversion of 42% with 1-indanol and indanone as main products (Table S2 in the ESM, Entry 1). The oxidation of tetralin affords a moderate conversion to α-tetralol and α-tetralone, possibly owing to the steric hindrance (Table S2 in the ESM, Entry 2). Co SACs also function for the oxidation of diphenylmethane and fluorene to corresponding products (benzophenone and fluoreone) with excellent selectivity (100%) in the reaction system (Table S2 in the ESM, Entry 3 and 4). When using 1, 3, 5-triethylbenzene as substrate, the oxidation will mainly proceed in one or two ethyl group with a high conversion (Table S2 in the ESM, Entry 5). Cumene can also be smoothly activated with a high conversion and selectivity with Co SACs (Table S2 in the ESM, Entry 6). Phenylcyclohexane is an important product in petrochemistry and the oxidation of phenylcyclohexane is a vital route to produce phenol [53]. The oxidation of phenylcyclohexane can also proceed towards 1-phenyl-cyclohexanol (Table S2 in the ESM, Entry 7).

To further understand the reaction mechanism, density functional theory (DFT) calculations are carried out setting oxidation of ethylbenzene as a model reaction. According to the results of NEXAFS analysis and element analysis test, the optimized geometry of Co SACs is constructed (Fig. 4(a) and Fig. S17(a) in the ESM) and used in the continuous calculations. The distances between cobalt and four coordinated nitrogen atoms are 1.917, 1.928, 2.125 and 2.158 Å, respectively suggesting the formation of only two Co–N covalent bonds (The calculated atomic radii for cobalt and nitrogen are 2.08 Å (1.52 Å for Co and 0.56 Å for N) [54]. Therefore, the coordination number of atomic Co sites is two, which is in good coincidence with experimental results. A possible pathway for the oxidation of ethylbenzene to acetophenone over Co SACs with O$_2$ as the oxidant was hypothesized based on the previous literature [55, 56]. According to the pathway, O$_2$ adsorbs on the surface by forming Co–O bond, while ethylbenzene adsorbs on the surface by dispersion force. In the first step, O$_2$@Co SACs abstracts one H atom from CH$_2$ group of ethylbenzene, with the formation of the phenylethyl and hydroperoxyl radicals. According to Gao's report [57], these two radicals are active intermediates of the process. Consequently, we focused on the first step only. Calculated initial, transition and final states are shown in Figs. 4(b)–4(d) and Figs. S17(b)–S17(d) in the ESM, respectively.
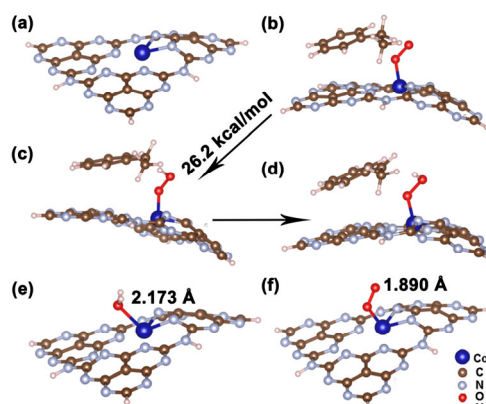
Table 1 Selective oxidation of ethylbenzene in air

Entry	Catalysts	Yield (%)^a	Sel. (%)		TOF (h^{-1})
			OH^b	C=O^c	
1	Co SACs	46	3	97	19.6
2^d	Co- porphyrin	ND			
3^d	Co NPs	ND			
4^e	Co SACs	ND			
5^f	Co SACs	ND			
6^g	Co SACs	42	1	99	17.9

Standard reaction conditions: ethylbenzene: 1 mL, catalyst: 2 mg, air atmosphere, temperature = 120 °C, reaction time = 24 h. ^{a}Con. and Sel. are determined by GC-FID with 100 μL dodecane as internal standard. ^{b}1-phenylethanol, ^{c}acetophenone, ^{d}catalyst (20 mg) was used. ^{e}Reaction in nitrogen atmosphere. ^{f}Hydroquinone (20 mg) was used. ^{g}Reaction after 5 runs.

Figure 4 DFT calculations of aerobic oxidation of styrene. (a) Optimized geometries of Co SACs. (b)–(d) Initial, transition and final states in the first elementary step of the proposed mechanism (Scheme S1 in the ESM). (e) and (f) Optimized geometries of O$_2$@Co SACs and H$_2$O@Co SACs, respectively.

The energy barrier for transition states is 26.2 kcal/mol, which suggests that the active intermediates (phenylethyl and hydroperoxyl radicals) are readily to be generated. Meanwhile, in the last step of the process, one H_2O molecule was generated. The optimized geometry of $H_2O@Co$ SACs is shown in Fig. 4(e) and Fig. S17(e) in the ESM. The distance between oxygen and cobalt is 2.173 Å, which is longer than corresponding Co–O bond in $O_2@Co$ SACs (Fig. 4(f) and Fig. S17(f) in the ESM, 1.890 Å). The calculated desorption energy for $H_2O@Co$ SACs is only 10.6 kcal/mol, which indicated that water molecule is easy to be desorbed and the center Co site cannot be poisoned.

4 Conclusion

In summary, we discovered a facile synthetic method to prepare Co SACs catalysts with a high metal loading of 23.58 wt.%. The high metal loading of Co SACs is chiefly attributed to the combined effects of low coordinated Co spices, high nitrogen content and high defect density. Surprisingly, Co SACs show excellent catalytic activity (19.6 h^{-1} TOF, 46% conversion and 97% selectivity) and stability (nearly no change after five runs) for oxidation of ethylbenzene in air. DFT calculations reveal that Co SACs show a low energy barrier in the first elementary step and a high resistance to water, which results in its robust catalytic performance. This work points out a possible way for practical applications of SACs catalysts.

Acknowledgements

Electronic Supplementary Material: Supplementary material (XAFS measurements and analysis details, computational details, XRD patterns, TEM, STEM, AFM and AC-HAADF-STEM images, XPS spectra, time-activity profile and rate constant plots) is available in the online version of this article at https://doi.org/10.1007/s12274-020-3244-4.

References

[1] Chu, L. L.; Lipshultz, J. M.; MacMillan, D. W. C. Merging photoredox and nickel catalysis: The direct synthesis of ketones by the decarboxylative arylation of α-Oxo acids. *Angew. Chem., Int. Ed.* 2015, 54, 7929–7933.

[2] Lesieur, M.; Genicot, C.; Pasau, P. Development of a flow photochemical aerobic oxidation of benzylic C–H bonds. *Org. Lett.* 2018, 20, 1987–1990.

[3] Clark, W. M.; Tickner-Eldridge, A. M.; Huang, G. K.; Pridgen, L. N.; Olsen, M. A.; Mills, R. J.; Lantos, I.; Baine, N. H. A Catalytic enantioselective synthesis of the endothelin receptor antagonists SB-209670 and SB-217242. A base-catalyzed stereospecific formal 1, 3-hydrogen transfer of a chiral 3-arylindenol. *J. Am. Soc. Chem.* 1998, 120, 4550–4551.

[4] Jana, S. K.; Wu, P.; Tatsumi, T. NiAl hydrotalcite as an efficient and environmentally friendly solid catalyst for solvent-free liquid-phase selective oxidation of ethylbenzene to acetophenone with 1 atm of molecular oxygen. *J. Catal.* 2006, 240, 268–274.

[5] Zhang, P. F.; Lu, H. F.; Zhou, Y.; Zhang, L.; Wu, Z. L.; Yang, S. Z.; Shi, H. L.; Zhu, Q. L.; Chen, Y. F.; Dai, S. Mesoporous $MnCeO_x$ solid solutions for low temperature and selective oxidation of hydrocarbons. *Nat. Commun.* 2015, 6, 8446.

[6] Wang, L.; Zhu, Y. H.; Wang, J. Q.; Liu, F. D.; Huang, J. F.; Meng, X. J.; Basset, J. M.; Han, Y.; Xiao, F. S. Two-dimensional gold nanostructures with high activity for selective oxidation of carbon–hydrogen bonds. *Nat. Commun.* 2015, 6, 6957.

[7] Zhang, P. F.; Gong, Y. T.; Li, H. R.; Chen, Z. R.; Wang, Y. Solvent-free aerobic oxidation of hydrocarbons and alcohols with Pd@N-doped carbon from glucose. *Nat. Commun.* 2013, 4, 1593.

[8] Biswas, R.; Das, S. K.; Bhaduri, S. N.; Bhaumik, A.; Biswas, P. AgNPs Immobilized over functionalized 2D hexagonal SBA-15 for catalytic C−H oxidation of hydrocarbons with molecular oxygen under solvent-free conditions. *ACS Sustainable Chem. Eng.* 2020, 8, 5856−5867.

[9] Kojima, T.; Nakayama, K.; Ikemura, K.; Ogura, T.; Fukuzumi, S. Formation of a ruthenium(IV)-Oxo complex by electron-transfer oxidation of a coordinatively saturated ruthenium(II) complex and detection of oxygen-rebound intermediates in C–H bond oxygenation. *J. Am. Chem. Soc.* 2011, 133, 11692–11700.

[10] Stubbs, A. W.; Dincă, M. Selective oxidation of C–H bonds through a manganese(III) hydroperoxo in Mn^{II}-Exchanged CFA-1. *Inorg. Chem.* 2019, 58, 13221−13228.

[11] Liu, L. C.; Corma, A. Metal catalysts for heterogeneous catalysis: From single atoms to nanoclusters and nanoparticles. *Chem. Rev.* 2018, 118, 4981–5079.

[12] Yao, Y. G.; Huang, Z. N.; Xie, P. F.; Wu, L. P.; Ma, L.; Li, T. Y.; Pang, Z. Q.; Jiao, M. L.; Liang, Z. Q.; Gao, J. L. et al. High temperature shockwave stabilized single atoms. *Nat. Nanotechnol.* 2019, 14, 851–857.

[13] Yang, J. R.; Li, W. H.; Wang, D. S.; Li, Y. D. Electronic metal-support interaction of single-atom catalysts and applications in electrocatalysis. *Adv. Mater.* 2020, 2003300.

[14] Yang, J. R.; Li, W. H.; Wang, D. S.; Li, Y. D. Single-atom materials: Small structures determine macroproperties. *Small Struct.* 2020, 2000051.

[15] Ji, S. F.; Qu, Y.; Wang, T.; Chen, Y. J.; Wang, G. F.; Li, X.; Dong, J. C.; Chen, Q. Y.; Zhang, W. Y.; Zhang, Z. D. et al. Rare-earth single erbium atoms for enhanced photocatalytic CO_2 reduction. *Angew. Chem., Int. Ed.* 2020, 59, 10651–10657.

[16] Shang, H. S.; Sun, W. M.; Sui, R.; Pei, J. J.; Zheng, L. R.; Dong, J. C.; Jiang, Z. L.; Zhou, D. N.; Zhuang, Z. B.; Chen, W. X. et al. Engineering isolated $Mn–N_2C_2$ atomic interface sites for efficient bifunctional oxygen reduction and evolution reaction. *Nano Lett.* 2020, 20, 5443−5450.

[17] Sun, T. T.; Li, Y. L.; Cui, T. T.; Xu, L. B.; Wang, Y. G.; Chen, W. X.; Zhang, P. P.; Zheng, T. Y.; Fu, X. Z.; Zhang, S. L. et al. Engineering of coordination environment and multiscale structure in single-site copper catalyst for superior electrocatalytic oxygen reduction. *Nano Lett.* 2020, 20, 6206−6214.

[18] Shang, H. S.; Wang, T.; Pei, J. J.; Jiang, Z. L.; Zhou, D. N.; Wang, Y.; Li, H. J.; Dong, J. C.; Zhuang, Z. B.; Chen, W. X. et al. Design of a single-atom indium$^{δ+}$-N_4 interface for efficient electroreduction of CO_2 to Formate. *Angew. Chem., Int. Ed.* 2020, https://doi.org/10.1002/anie.202010903.

[19] Tian, S.; Hu, M.; Xu, Q.; Gong, W. B.; Chen, W. X.; Yang, J. R.; Zhu, Y. Q.; Chen, C.; He, J.; Liu, Q. et al. Single-atom Fe with Fe_1N_3 structure showing superior performances for both hydrogenation and transfer hydrogenation of nitrobenzene. *Sci. China Mater.* 2020, https://doi.org/10.1007/s40843-020-1443-8.

[20] Zhuang, Z. C.; Kang, Q.; Wang, D. S.; Li, Y. D. Single-atom catalysis enables long-life, high-energy lithium-sulfur batteries. *Nano Res.* 2020, 13, 1856–1866.

[21] Xiong, Y.; Sun, W. M.; Xin, P. Y.; Chen, W. X.; Zheng, X. S.; Yan, W. S.; Zheng, L. R.; Dong, J. C.; Zhang, J.; Wang, D. S. et al. Gram-scale synthesis of high-loading single-atomic-site Fe catalysts for effective epoxidation of styrene. *Adv. Mater.* 2020, 32, 2000896.

[22] Zhang, J.; Zheng, C. Y.; Zhang, M. L.; Qiu, Y. J.; Xu, Q.; Cheong, W. C.; Chen, W. X.; Zheng, L. R.; Gu, L.; Hu, Z. P. et al. Controlling N-doping type in carbon to boost single-atom site Cu catalyzed transfer hydrogenation of quinoline. *Nano Res.* 2020, 13, 3082–3087.

[23] Li, X. Y.; Rong, H. P.; Zhang, J. T.; Wang, D. S.; Li, Y. D. Modulating the local coordination environment of single-atom catalysts for enhanced catalytic performance. *Nano Res.* **2020**, *13*, 1842–1855.

[24] Liu, J. Y. Catalysis by supported single metal atoms. *ACS Catal.* **2017**, *7*, 34−59.

[25] Zhang, N. Q.; Ye, C. L.; Yan, H.; Li, L. C.; He, H.; Wang, D. S.; Li, Y. D. Single-atom site catalysts for environmental catalysis. *Nano Res.* **2020**, *13*, 3165–3182.

[26] Chen, Y. J.; Gao, R.; Ji, S. F.; Li, H. J.; Tang, K.; Jiang, P.; Hu, H. B.; Zhang, Z. D.; Hao, H. G.; Qu, Q. Y. et al. Atomic-level modulation of electronic density of metal-organic frameworks-derived Co single-atom sites to enhance oxygen reduction performance. *Angew. Chem., Int. Ed.* **2020**, DOI: 10.1002/ange.202012798.

[27] Cui, X. J.; Li, W.; Ryabchuk, P.; Junge, K.; Beller, M. Bridging homogeneous and heterogeneous catalysis by heterogeneous single-metal-site catalysts. *Nat. Catal.* **2018**, *1*, 385–397.

[28] Mao, J. J.; He, C. T.; Pei, J. J.; Liu, Y.; Li, J.; Chen, W. X.; He, D. S.; Wang, D. S.; Li, Y. D. Isolated Ni atoms dispersed on Ru nanosheets: High-performance electrocatalysts toward hydrogen oxidation reaction. *Nano Lett.* **2020**, *20*, 3442–3448.

[29] Sun, T. T.; Xu, L. B.; Wang, D. S.; Li, Y. D. Metal organic frameworks derived single atom catalysts for electrocatalytic energy conversion. *Nano Res.* **2019**, *12*, 2067–2080.

[30] Zhang, T.; Zhang, D.; Han, X. H.; Dong, T.; Guo, X. W.; Song, C. S.; Si, R.; Liu, W.; Liu, Y. F.; Zhao, Z. K. Preassembly strategy to fabricate porous hollow carbonitride spheres inlaid with single Cu–N₃ sites for selective oxidation of benzene to phenol. *J. Am. Chem. Soc.* **2018**, *140*, 16936–16940.

[31] Li, J. K.; Pršlja, P.; Shinagawa, T.; Fernández, A. J. M.; Krumeich, F.; Artyushkova, K.; Atanassov, P.; Zitolo, A.; Zhou, Y. C.; García-Muelas, R. et al. Volcano trend in electrocatalytic CO₂ reduction activity over atomically dispersed metal sites on nitrogen-doped carbon. *ACS Catal.* **2019**, *9*, 10426−10439.

[32] Cao, Y. J.; Chen, S.; Luo, Q. Q.; Yan, H.; Lin, Y.; Liu, W.; Cao, L. L.; Lu, J. L.; Yang, J. L.; Yao, T. et al. Atomic-level insight into optimizing the hydrogen evolution pathway over a Co₁-N₄ single-site photocatalyst. *Angew. Chem., Int. Ed.* **2017**, *56*, 12191–12196.

[33] Gong, W. B.; Yuan, Q. L.; Chen, C.; Lv, Y.; Lin, Y.; Liang, C. H.; Wang, G. Z.; Zhang, H. M.; Zhao, H. J. Liberating N-CNTs confined highly dispersed Co-Nₓ sites for selective hydrogenation of quinolines. *Adv. Mater.* **2019**, *31*, 1906051.

[34] Wan, J. W.; Zhao, Z. H.; Shang, H. S.; Peng, B.; Chen, W. X.; Pei, J. J.; Zheng, L. R.; Dong, J. C.; Cao, R.; Sarangi, R. et al. *In situ* phosphatizing of triphenylphosphine encapsulated within metal−organic frameworks to design atomic Co₁−P₁N₃ interfacial structure for promoting catalytic performance. *J. Am. Chem. Soc.* **2020**, *142*, 8431−8439.

[35] Ye, M. Y.; Li, S.; Zhao, X. J.; Tarakina, N. V.; Teutloff, C.; Chow, W. Y.; Bittl, R.; Thomas, A. Cobalt-exchanged poly(heptazine imides) as transition metal–Nₓ electrocatalysts for the oxygen evolution reaction. *Adv. Mater.* **2020**, *32*, 1903942.

[36] Ou H. H.; Wang, D. S.; Li, Y. D. How to select effective electrocatalysts: Nano or single atom? *Nano Select* **2020**, https://doi.org/10.1002/nano.202000239.

[37] Zhao, Q.; Yao, W. F.; Huang, C. P.; Wu, Q.; Xu, Q. J. Effective and durable Co single atomic Co catalysts for photocatalytic hydrogen production. *ACS Appl. Mater. Interfaces.* **2017**, *9*, 42734–42741.

[38] Zitolo, A.; Ranjbar-Sahraie, N.; Mineva, T.; Li, J. K.; Jia, Q. Y.; Stamatin, S.; Harrington, G. F.; Lyth, S. M.; Krtil, P.; Mukerjee, S. et al. Identification of catalytic sites in cobalt-nitrogen-carbon materials for the oxygen reduction reaction. *Nat. Commun.* **2017**, *8*, 957.

[39] Fei, H. L.; Dong, J. C.; Arellano-Jiménez, M. J.; Ye, G. L.; Kim, N. D.; Samuel, E. L. G; Peng, Z. W.; Zhu, Z.; Qin, F.; Bao, J. M. et al. Atomic cobalt on nitrogen-doped graphene for hydrogen generation. *Nat. Commun.* **2015**, *6*, 8668.

[40] Yue, X. Y.; Li, X. L.; Wang, W. W.; Chen, D.; Qiu, Q. Q.; Wang, Q. C.; Wu, X. J.; Fu, Z. W.; Shadike, Z.; Yang, X. Q. et al. Wettable carbon felt framework for high loading Li-metal composite anode. *Nano Energy* **2019**, *60*, 257–266.

[41] Zhu, Y. F.; Kong, X.; Yin, J. Q.; You, R.; Zhang, B.; Zheng, H. Y.; Wen, X. D.; Zhu, Y. L.; Li, Y. W. Covalent-bonding to irreducible SiO₂ leads to high-loading and atomically dispersed metal catalysts. *J. Catal.* **2017**, *353*, 315–324.

[42] Kunwar, D.; Zhou, S. L.; DeLaRiva, A.; Peterson, E. J.; Xiong, H. F.; Pereira-Hernández, X. I.; Purdy, S. C.; ter Veen, R.; Brongersma, H. H.; Miller, J. T. et al. Stabilizing high metal loadings of thermally stable platinum single atoms on an industrial catalyst support. *ACS Catal.* **2019**, *9*, 3978–3990.

[43] Cao, J. Y.; Du, C.; Wang, S. C.; Mercier, P.; Zhang, X. G.; Yang, H.; Akins, D. L. The production of a high loading of almost monodispersed Pt nanoparticles on single-walled carbon nanotubes for methanol oxidation. *Electrochem. Commun.* **2007**, *9*, 735–740.

[44] Wang, Y. M.; Zou, L. L.; Huang, Q. H.; Zou, Z. Q.; Yang, H. 3D carbon aerogel-supported PtNi intermetallic nanoparticles with high metal loading as a durable oxygen reduction electrocatalyst. *Int. J. Hydrogen Energy.* **2017**, *42*, 26695–26703.

[45] Yin, P. Q.; Yao, T.; Wu, Y. E.; Zheng, L. R.; Lin, Y.; Liu, W.; Ju, H. X.; Zhu, J. F.; Hong, X.; Deng, Z. X. et al. Single cobalt atoms with precise N-coordination as superior oxygen reduction reaction catalysts. *Angew. Chem., Int. Ed.* **2016**, *55*, 10800–10805.

[46] Xu, J.; Zhang, L. W.; Shi, R.; Zhu, Y. F. Chemical exfoliation of graphitic carbon nitride for efficient heterogeneous photocatalysis. *J. Mater. Chem. A* **2013**, *1*, 14766–14772.

[47] Wu, H. H.; Li, H. B.; Zhao, X. F.; Liu, Q. F.; Wang, J.; Xiao, J. P.; Xie, S. H.; Si, R.; Yang, F.; Miao, S. et al. Highly doped and exposed Cu(I)–N active sites within graphene towards efficient oxygen reduction for zinc–air batteries. *Energy Environ. Sci.* **2016**, *9*, 3736–3745.

[48] Khabashesku, V. N.; Zimmerman, J. L.; Margrave, J. L. Powder synthesis and characterization of amorphous carbon nitride. *Chem. Mater.* **2000**, *12*, 3264–3270.

[49] Bertoncello, R.; Bettinelli, M.; Casarin, M.; Gulino, A.; Tondello, E.; Vittadini, A. Hexakis(acetato)oxotetrazinc, a well-tailored molecular model of zinc oxide. An experimental and theoretical investigation of the electronic structure of Zn₄O(acetate)₆ and ZnO by means of UV and X-ray photoelectron spectroscopies and first principle local density molecular cluster calculations. *Inorg. Chem.* **1992**, *31*, 1558–1565.

[50] Zhou, J. G.; Zhou, X. T.; Li, R. Y.; Sun, X. L.; Ding, Z. F.; Cutler, J.; Sham, T. K. Electronic structure and luminescence center of blue luminescent carbon nanocrystals. *Chem. Phys. Lett.* **2009**, *474*, 320–324.

[51] Liang, Y. Y.; Wang, H. L.; Zhou, J. G.; Li, Y. G.; Wang, J.; Regier, T.; Dai, H. J. Covalent hybrid of spinel manganese–cobalt oxide and graphene as advanced oxygen reduction electrocatalysts. *J. Am. Soc. Chem.* **2012**, *134*, 3517–3523.

[52] Lv, W. M.; Yang, L.; Fan, B. B.; Zhao, Y.; Chen, Y. F.; Lu, N. Y.; Li, R. F. Silylated MgAl LDHs intercalated with MnO₂ nanowires: Highly efficient catalysts for the solvent-free aerobic oxidation of ethylbenzene. *Chem. Eng. J.* **2015**, *263*, 309–316.

[53] Sun, W. Z.; Zhang, S. L.; Qiu, J. F.; Xu, Z. M.; Zhao, L. Modeling the liquid phase autoxidation of cyclohexylbenzene to hydroperoxide. *Chem. Eng. Res. Des.* **2017**, *124*, 202–210.

[54] Clementi, E.; Raimondi, D. L.; Reinhardt, W. P. Atomic screening constants from SCF functions. II. Atoms with 37 to 86 electrons. *J. Chem. Phys.* **1967**, *47*, 1300–1307.

[55] Devika, S.; Palanichamy, M.; Murugesan, V. Selective oxidation of ethylbenzene over CeAlPO-5. *Appl. Catal. A Gener.* **2011**, *407*, 76–84.

[56] Ricca, C.; Labat, F.; Russo, N.; Adamo, C.; Sicilia, E. Oxidation of ethylbenzene to acetophenone with N-Doped graphene: Insight from theory. *J. Phys. Chem. C* **2014**, *118*, 12275–12284.

[57] Gao, Y. J.; Hu, G.; Zhong, J.; Shi, Z. J.; Zhu, Y. S.; Su, D. S.; Wang, J. G.; Bao, X. H.; Ma, D. Nitrogen-doped sp²-hybridized carbon as a superior catalyst for selective oxidation. *Angew. Chem., Int. Ed.* **2013**, *52*, 2109–2113.